

Growth Evolution of AZO thin Films Deposited by Magnetron Sputtering at Room Temperature

R. Ramos^a , M. Chaves^b, E. Martins^a, Steven F. Durrant^a , E.C. Rangel^a, T.F. da Silva^c,
J.R.R. Bortoleto^{a*} 

^aUniversidade Estadual Paulista (UNESP), Av. 3 Março, 511, Sorocaba, SP, Brasil.

^bUniversidade de Sorocaba, Sorocaba, SP, Brasil.

^cUniversidade de São Paulo (USP), Rua do Matão Trav. R187, São Paulo, SP, Brasil.

Received: January 19, 2021; Revised: February 24, 2021; Accepted: June 16, 2021

Thin AZO films were grown by RF magnetron sputtering for different deposition times in argon plasmas. Optical, structural, and morphological properties, together with elemental composition, were studied and correlated with the observed effects on the electrical properties and compared with two models of mobility scattering (ionized impurities and grain boundaries). The results suggest that the carrier density in the studied case is limited to below 15% owing to the low ionization efficiency caused by the formation of neutral impurities as homologous phases. While the spread in the mobility during the initial stages of film growth is strongly influenced by grain boundaries, in thicker films the limitation on ion efficiency becomes more significant.

Keywords: ZnO, Al thin films, TCO, morphological properties.

1. Introduction

Transparent conducting oxides (TCO's) can transmit light in the visible (3.1 to 1.8 eV) and conduct electricity without either property being degraded. Such properties are usually antagonistic and require an optimization so that they can be exploited together¹. These materials have attracted interest owing to their diverse applications, amongst others, to optoelectronics, magnetoelectronics, photonics, thermoelectronics, piezoelectronics, and as sensors, in energy generation, low emissivity windows, and flexible displays².

Until now, the most used TCO is indium-doped tin oxide (ITO), which presents high transmission in the visible and an electrical resistivity of up to 120 $\mu\Omega\text{cm}$ ^{3,4}, but its high cost and toxicity and the scarcity of indium drive the search for alternative materials.

Among TCO's, zinc oxide (ZnO) is versatile owing to its properties such as a direct high energy band-gap (~ 3.3 eV), high exciton binding energy (60 meV)⁵, as well as being a material composed of cheap, abundant, non-toxic elements, and readily deposited by several techniques⁶⁻⁹. ZnO is an intrinsic n-type semiconducting material, and to improve its electrical properties a dopant that provides charge carriers is used. Doping with Al has been employed by several authors¹⁰⁻¹⁶ to reduce the electrical resistivity of ZnO, arriving at values of 230 $\mu\Omega\text{cm}$ for depositions using DC magnetron sputtering at 270 °C. The thin film properties of AZO (ZnO:Al) depend strongly on the deposition parameters used, such as deposition time, temperature, total pressure in the chamber, applied power, substrate temperature and also the post-deposition annealing temperature^{17,18}.

The present work aims to study the evolution of the growth of AZO films and how changes in the structural properties influence the electrical and optical properties. Surface texturing of the films is also examined because one way to increase the energetic efficiency of photovoltaic devices is to imprison the light in the upper layer of solar cells^{19,20}.

2. Experimental Details

The ZnO:Al films were deposited on substrates of silicon and glass, using RF magnetron sputtering. Before deposition, the substrates were cleaned in an ultrasonic bath (Ultrasonic Clear CBU-100) in deionized water and isopropyl alcohol for 480 seconds in each step and were dried with a thermal blower. The sputtering system employed consisted of a chamber made from 304 stainless-steel of 270 mm diameter and 200 mm height, evacuated by a turbo molecular pump (Edwards T-Station 75). A ZnO:Al (Al₂O₃ 2 wt.%) ceramic target of 99.95% purity was used to synthesize films at room temperature (RT).

A fixed target to substrate distance of 30 mm was used. The plasma was maintained by a radiofrequency supply (13.56 MHz) connected to the target and the sputtering gas was argon, fed to the chamber via a flowmeter (MKS 1179A) at 1.5 sccm, corresponding to a pressure of 1 mTorr. All the films were grown at an RF power of 100 W, varying the deposition time between 30 s and 40 min.

The crystalline structure of the films was analyzed employing an X-ray Diffractometer (Panalytical X'Pert Powder), using the ω -scan geometry with CuK $_{\alpha}$ radiation of wavelength, λ , 1.5405 Å, incident at 2° relative to the sample surface. To track changes in morphology and roughness (rms) an atomic force microscope (XE-100 Park Systems) operating in the non-

*e-mail: jose.rr.bortoleto@unesp.br

contact mode, employing a silicon tip of 5 nm nominal radius, with scans over $2\ \mu\text{m} \times 2\ \mu\text{m}$, and a field-emission scanning electron microscope (Jeol JSM 7500F) were used. A Veeco Instruments (Dektak 150) profilometer was used to measure the film thickness. Quantitative investigation of the elements Zn, O and Al was undertaken using Rutherford Back-Scattering, RBS, with a 2.2 MeV He^+ beam. To characterize the AZO films as TCOs, their optical and electrical properties were studied by Ultraviolet-visible infrared Spectroscopy, UVS, using a Perkin Elmer Lambda 750 spectrometer (λ from 190 to 3300 nm) and electrical resistivity was measured using the four-point method.

3. Results and Discussions

3.1. Composition and Structural Properties

Figure 1 shows the deposition rate, calculated from the film thickness and the deposition time, as a function of the deposition time, revealing a slightly higher rate in the early stages of film growth, stabilizing after about 2.5 min.

Figure 2 shows the chemical composition (in at.%) of the films measured by RBS. In the initial growth stages, i.e. at small thicknesses, there is an increase in [O], such that it is almost twice that of [Zn]. As the film thickness increases, there is a reduction in [O] and an increase in [Zn], and from 270 nm the ratio of the concentrations of these elements stabilizes. The concentration of Al is uniform beyond about a thickness of 50 nm.

The diffractogram and the extracted information are shown in Figure 3a and 3b, respectively. Poor structural quality is exhibited by the films of 30 nm and 50 nm, as indicated by the low counts in the diffraction peaks. From a thickness of 80 nm, all the samples show diffraction peaks in the (002) plane, characteristic of the hexagonal wurtzite structure^{21,22}, with preferential orientation in the *c*-axis perpendicular to the substrate^{21,23}.

Under the same data acquisition conditions, the intensity of the peak associated with the (002) orientation increases with increasing pressure, and other peaks associated with the (101), (102) and (103) planes appear, indicating that growth also occurs in other crystallographic planes.

The strain in the initial stages of growth tends to be greater because of the strong film-substrate interaction, typical of island growth. When the islands begin to coalesce, the strain tends to be released.

AZO crystallites deposited by the described method at a lower deposition temperature are larger than those of ZnO reported in the literature²⁴.

The diffraction angle of the (002) plane increases from 33.89° to 34.15° , indicating that as the film thickness increases, the residual stress decreases. In addition, the full width at half maximum (FWHM) of the (002) peaks decrease, which may be attributed to an improvement in the structural quality of the crystallites²⁵. The FWHM is related to the crystallite size via the Scherrer equation²⁶

$$D = \frac{0.9\lambda}{(B_m - B_s) \cos\theta} \quad (1)$$

where $\lambda = 0.15406\ \text{nm}$, B_m and B_s are the experimental and instrumental FWHM of the peak used, respectively. From

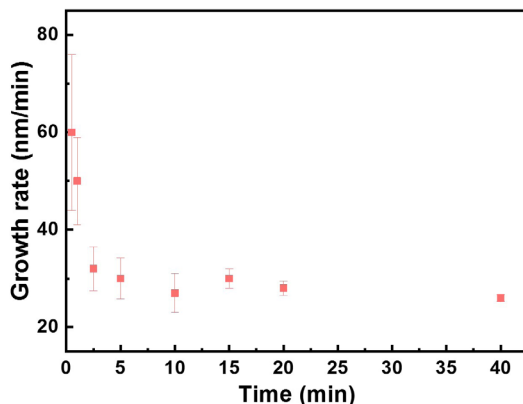


Figure 1. Deposition rate as a function of deposition time.

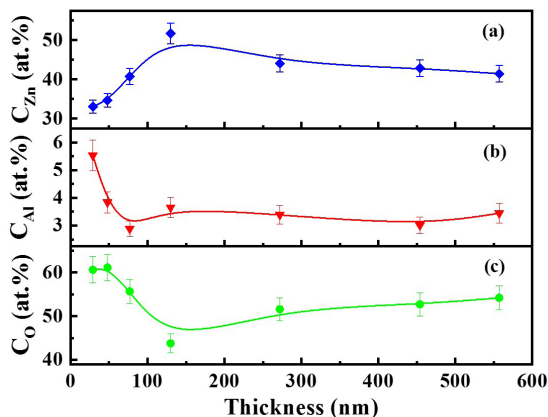


Figure 2. Concentrations of (a) Zn, (b) Al and (c) O measured using RBS.

this analysis, the crystallite size increases with film thickness, stabilizing from a thickness of 80 nm.

3.2. Surface Morphology

Figure 4 shows AFM images and the respective mean square roughnesses. In the first stages of growth the film is in the process of nucleation, forming islands of the material produced during sputtering, and the roughness is close to that of the substrate. As the islands grow, they begin to encroach on each other, resulting in the coalescence phase. A more regular distribution of grains leads to more vertical growth, increasing the roughness.

As revealed in the micrographs of Figure 5a, the initial stage of film growth presents a structure composed of small grains. As the film thickness increases, the structure grows horizontally, touching at the grain boundaries and producing a larger structure. The structure then grows in columns, having a growth preference in certain faces of the crystalline unit cell. As shown in Figure 5b, such structures are formed by crystallites. The profiles extracted from the AFM measurements were included (not to scale) to show schematically the growth in roughness observed as the thickness increases.

3.3. Optical and electrical properties

The transmission spectra of the films, shown in Figure 6, reveal that the optical transmittance is about 80% in the visible

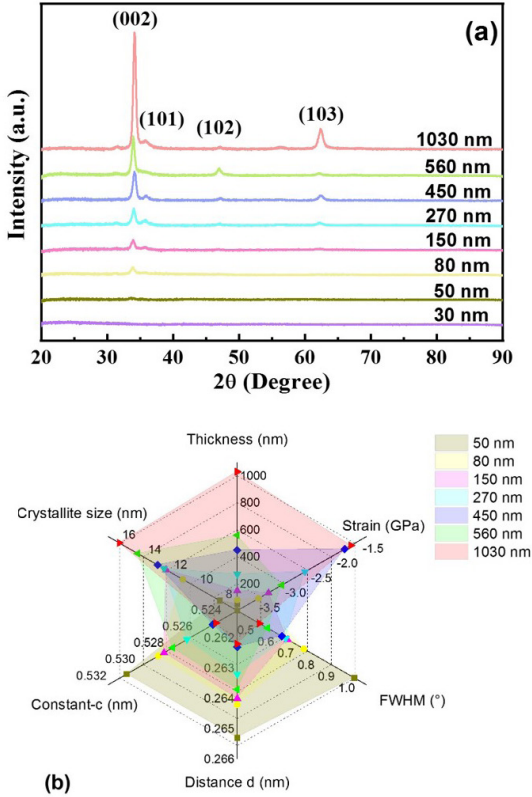


Figure 3. (a) Grazing incidence X-ray diffraction spectra of the AZO films deposited for different sputtering times. (b) Parameters extracted from the diffractogram together with the film thickness.

region. Interference bands are visible in this region and are caused by multiple reflections in the film. In the ultraviolet, there is an abrupt change called the absorption edge, caused by interband transitions that occur in the film, and is related to the band gap, found by the Tauc method^{27,28}, presented in Table 1. The gaps are greater than that of pure ZnO (3.26 eV)²⁹. The increase may be explained by the Burstein-Moss effect³⁰, in which high impurity doping fills empty states in the conduction band, causing an increase in the gap energy of the AZO films^{31,32}.

For infrared wavelengths, absorption is usually attributed to plasmon oscillations (oscillations of free charges)¹; however, observation of the carrier density in the samples shows that it is almost constant, and calculation of the wavelength of the plasmons yields 3250 nm. The reduction in the transmittance is caused by greater film thickness.

In one mole of ZnO there are 4.148×10^{22} molecules/cm³, and considering that each Al atom contributes one electron to the carrier density, via the relation among the metals ($[Al]/([Al]+[Zn])$) the electron density, n_e , may be obtained:

$$n_e = \frac{[Al]}{[Al]+[Zn]} 4.148 \times 10^{22} \quad (2)$$

Comparing the free electron density and that calculated from the Hall effect the ionization efficiency may be found, as shown in Table 1, and indicates the percentage of Al atoms contributing to electrical conduction.

In the early stages of growth, the film begins to form as small crystals with different crystalline orientations that slowly increase in size until the grain boundaries touch, then growing vertically in a process described as evolutionary

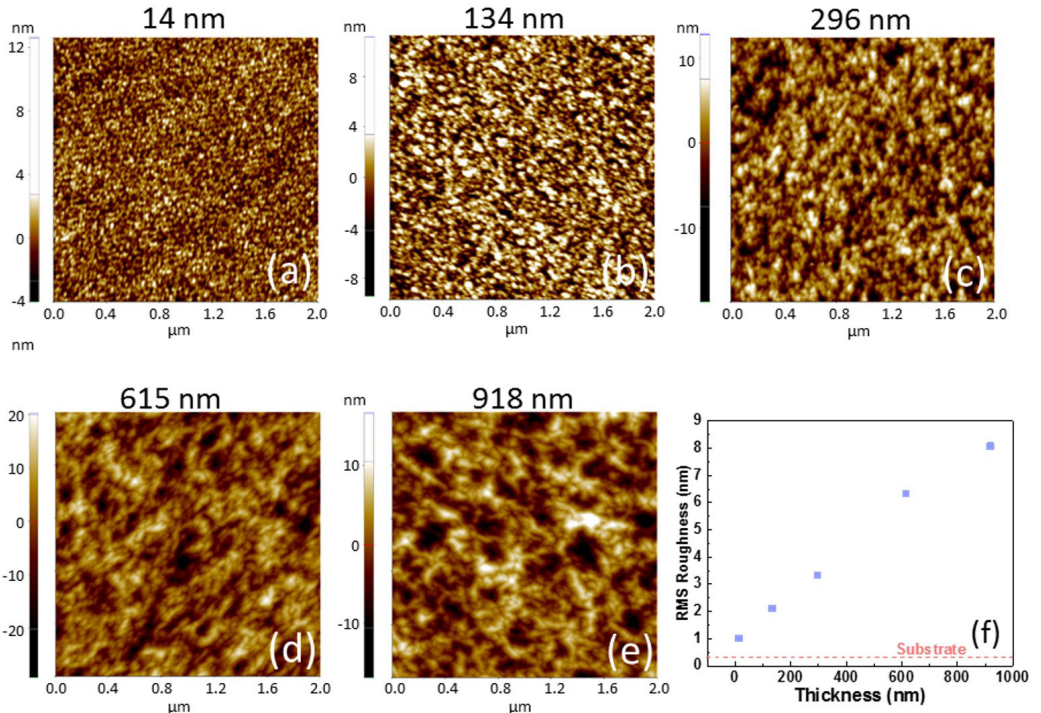


Figure 4. AFM images of samples of different thickness (a) 14 nm (b) 134 nm (c) 296 nm (d) 615 nm (e) 918 nm and their (f) RMS roughness. The roughness increases with increasing thickness.

Table 1. Optical band gap calculated from the transmittance spectral data, and the Al-doping efficiency calculated from the RBS and Hall effect measurements as a function of film thickness.

Thickness (nm)	30	50	80	150	270	450	560	1030
Optical Gap (eV)	3.35	3.42	3.55	3.58	3.59	3.59	3.65	3.59
Al-doping efficiency (%)	1.46	4.13	11.08	12.95	13.62	13.62	17.78	12.35

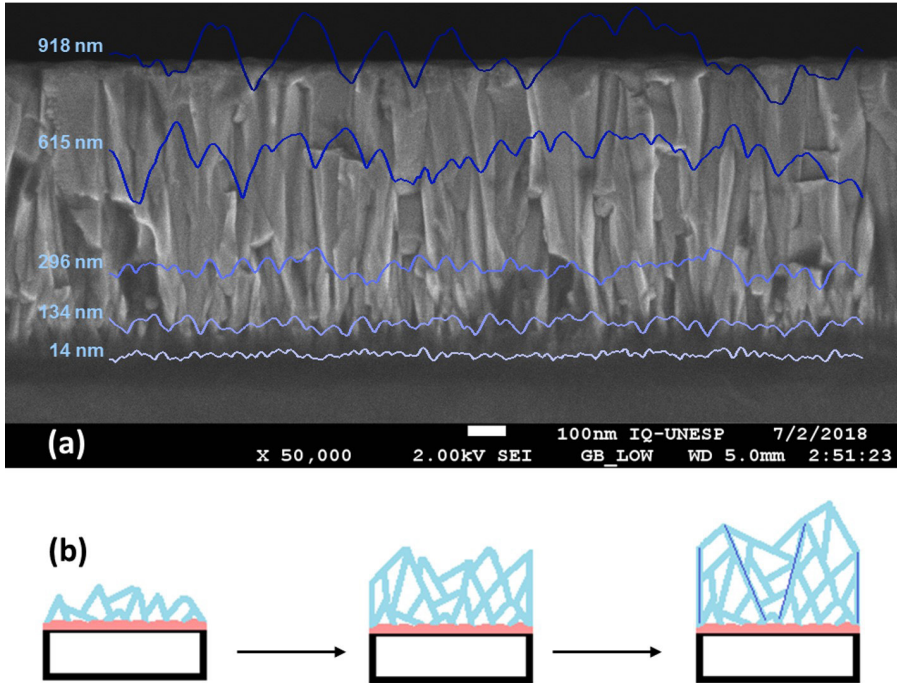


Figure 5. (a) Scanning electron micrographs; (b) AFM-derived schematic profiles (not to scale), illustrating how the film structure changes with growth.

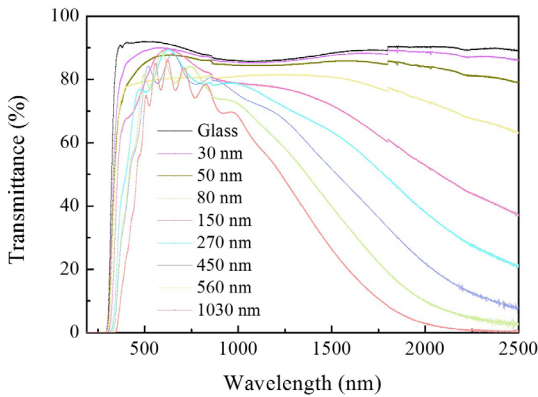


Figure 6. Optical transmittance spectra of the AZO films deposited onto glass substrates for different sputtering times. A typical spectrum of the glass substrate is also shown.

selection³³, where the grains grow more rapidly in the direction normal to the substrate surface and coalesce with the other grains, forming a wormlike structure, increasing laterally and reducing the density of boundaries³⁴.

At high deposition rates, short times are insufficient to produce a continuous, homogeneous film^{32,35}, such that the microstructure formed tends to absorb more oxygen, causing the confinement of charge carriers and a decrease in their mobility and concentration on the surface³⁶.

The experimental mobility, μ_{exp} , may be expressed as:

$$\frac{1}{\mu_{exp}} = \frac{1}{\mu_{ii}} + \frac{1}{\mu_N} + \frac{1}{\mu_{GB}} + \frac{1}{\mu_{PS}} \quad (3)$$

where μ_{ii} is the scattering by ionized impurities, μ_N is the scattering by neutral impurities, μ_{GB} is the scattering by grain boundaries and μ_{PS} is the scattering by phonons.

Observe in Figure 7 that for the film of 30 nm, the resistivity is high, owing to the poor structural quality, which increases the contribution of scattering centers such as grain boundaries, and a large amount of oxygen and aluminum that neutralize the carriers produced by extrinsic doping according to the data on Al-doping efficiency, thus contributing as a neutral scattering center.

Below a thickness of 80 nm, the carrier density and mobility increase, where the reduction in [O] and the increase in grain size presented in Figure 2c and Figure 7, respectively, justify the improvement in the electrical resistivity. In this region, the contributions by grain boundary scattering³⁷ and by neutral impurities become more significant.

For thicknesses above 80 nm, the carrier density and mean grain size become almost constant as a function of film thickness. Thus the contribution to scattering by grain boundaries and neutral impurities may be considered constant, and the degradation in mobility is more influenced by scattering by ionized impurities^{3,38} and by phonons³⁴.

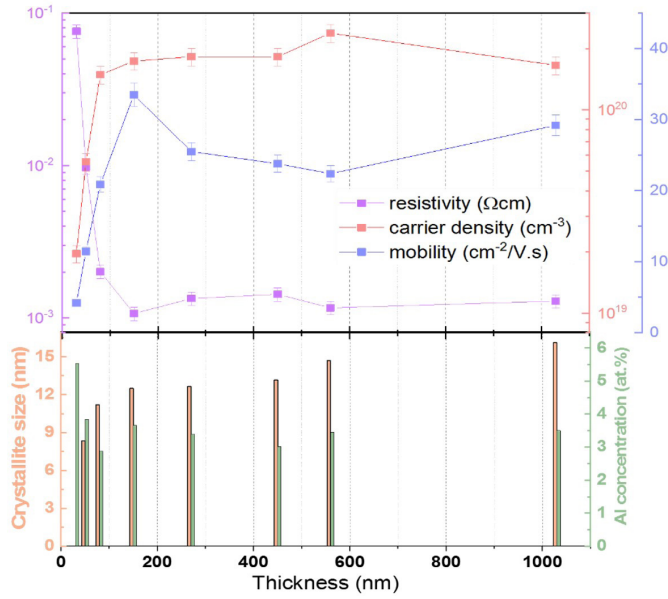


Figure 7. Electrical properties (top), crystallite size (bottom left), Al concentration (bottom right).

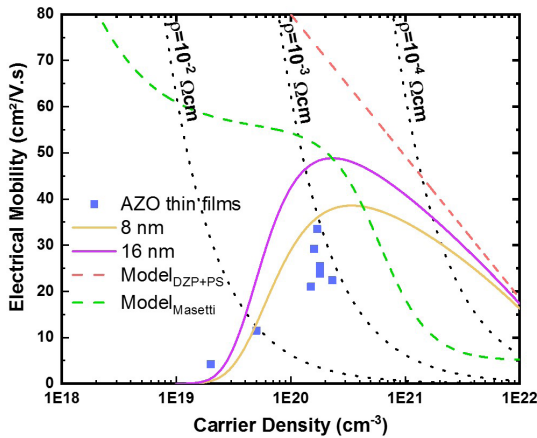


Figure 8. Experimental electrical mobility and theoretical mobility obtained by the DPZ+PS model³⁷, and the Masetti model³⁸, as a function of the carrier density.

Figure 8 shows a plot of the contributions of the DZP model (ionized impurities and phonons)³⁷ and the Masetti model (ionized impurities)^{34,38} in the lattice, together with the experimental data of samples. The dotted lines show the regions where the resistivity is 10^{-4} , 10^{-3} and 10^{-2} Ωcm . The curves marked 8 nm and 16 nm (crystallite size) were produced considering the DZP + PS models³⁷ and the scattering by grain boundaries³⁴, based on the experimental mobility Equation 3. The experimental points are limited above by scattering from ionized impurities and by grain boundaries, and to the right they are limited by the formation of neutral impurities, which limit the ionization efficiency and consequently reduce the carrier density.

Depending on the deposition technique, the solubility of Al in ZnO has a limit (in at.%). Above this limit, some

studies indicate the formation of a metastable homologous phase, ZnAl_2O_4 ^{39,40}, thus increasing the formation of neutral clusters. The low ionization efficiency is caused by neutral impurities that may be caused by the formation of homologous phases, such as ZnAl_2O_4 or $\text{ZnO-Al}_2\text{O}_3$. These phases, however, do not present sufficient signals to be detected by the conventional XRD used in the present study.

4. Conclusions

The electrical and optical properties were evaluated according to the growth of the thin film. At the beginning of growth, the film did not present a crystalline structure sufficient to be identified using XRD, and no well-defined structures were revealed by SEM. As the thickness increased, small crystallites began to be formed and organized into structures. The crystallites exhibit a small increase in size as revealed by XRD and columnar structures begin to appear. The carrier density is limited to 15% of the total of dopants owing to the low ionization efficiency. According to electrical measurements and theoretical curves, the electrical resistivity of the material in addition to being influenced by ionized impurities and grain boundaries, is modified by passivating traps of charge and homologous phases, generated by dopants that do not effectively contribute to the carrier density and consequently to the electrical conductivity of the material.

5. Acknowledgements

The authors thank the Brazilian agency CNPq (Proc. 555774/2010-4 and 301622/2012-4) for financial support. This study was financed in part by the Coordenação de Aperfeiçoamento de Pessoal de Nível Superior - Brasil (CAPES) - Finance Code 001 and 1795290/2018.

6. References

1. Ellmer K. Past achievements and future challenges in the development of optically transparent electrodes. *Nat Photonics*. 2012;6:809-17.
2. Lorenz M, Ramachandra Rao MS, Venkatesan T, Fortunato E, Barquinha P, Branquinho R, et al. The 2016 oxide electronic materials and oxide interfaces roadmap. *J Phys D Appl Phys*. 2016;49:433001.
3. Ellmer K, Mientus R. Carrier transport in polycrystalline transparent conductive oxides: a comparative study of zinc oxide and indium oxide. *Thin Solid Films*. 2008;516(14):4620-7.
4. Minami T. Transparent conducting oxide semiconductors for transparent electrodes. *Semicond Sci Technol*. 2005;20:S35-44.
5. Kolodziejczak-Radzimska A, Jesionowski T. Zinc oxide—from synthesis to application: a review. *Materials (Basel)*. 2014;7(4):2833-81.
6. Fan JC, Sreekanth KM, Xie Z, Chang SL, Rao KV. p-Type ZnO materials: theory, growth, properties and devices. *Prog Mater Sci*. 2013;58(6):874-985.
7. An HR, Ahn HJ, Park JW. High-quality, conductive, and transparent Ga-doped ZnO films grown by atmospheric-pressure chemical-vapor deposition. *Ceram Int*. 2015;41(2):2253-9.
8. Rahmane S, Aida MS, Djouadi MA, Barreau N. Effects of thickness variation on properties of ZnO:Al thin films grown by RF magnetron sputtering deposition. *Superlattices Microstruct*. 2015;79:148-55.
9. Prabukanthan P, Harichandran G. Effect of 100 MeV O⁷⁺ ion beam irradiation on radio frequency reactive magnetron sputtered ZnO thin films. *Mater Sci Semicond Process*. 2013;16(1):193-9.
10. Jo GH, Kim SH, Koh JH. Enhanced electrical and optical properties based on stress reduced graded structure of Al-doped ZnO thin films. *Ceram Int*. 2018;44:735-41.
11. Kluth O, Schöpe G, Rech B, Menner R, Oertel M, Orgassa K, et al. Comparative material study on RF and DC magnetron sputtered ZnO:Al films. *Thin Solid Films*. 2006;502(1-2):311-6.
12. Jäger S, Szyszka B, Szczyrbowski J, Bräuer G. Comparison of transparent conductive oxide thin films prepared by a.c. and d.c. reactive magnetron sputtering. *Surf Coat Tech*. 1998;98(1-3):1304-14.
13. Misra P, Ganeshan V, Agrawal N. Low temperature deposition of highly transparent and conducting Al-doped ZnO films by RF magnetron sputtering. *J Alloys Compd*. 2017;725:60-8.
14. Szyszka B. Transparent and conductive aluminum doped zinc oxide films prepared by mid-frequency reactive magnetron sputtering. *Thin Solid Films*. 1999;351(1-2):164-9.
15. Paul B, Singh B, Ghosh S, Roy A. A comparative study on electrical and optical properties of group III (Al, Ga, In) doped ZnO. *Thin Solid Films*. 2016;603:21-8.
16. Minami T, Ohtani Y, Miyata T, Kuboi T. Transparent conducting Al-doped ZnO thin films prepared by magnetron sputtering with dc and rf powers applied in combination. *J Vac Sci Technol A*. 2007;25(4):1172-7.
17. Jeong SH, Boo JH. Influence of target-to-substrate distance on the properties of AZO films grown by RF magnetron sputtering. *Thin Solid Films*. 2004;447-448:105-10.
18. Hsu CY, Kao LM, Lin YC. Effect of deposition parameters and annealing temperature on the structure and properties of Al-doped ZnO thin films. *Mater Chem Phys*. 2010;124:330-5.
19. Owen JI, Zhang W, Köhl D, Hüpkens J. Study on the in-line sputtering growth and structural properties of polycrystalline ZnO:Al on ZnO and glass. *J Cryst Growth*. 2012;344(1):12-8.
20. Wang Y, Song J, Niu G, Yang Z, Wang Z, Meng X, et al. Fabrication and post-chemical-etched surface texturing of H and Ti co-doped ZnO film for silicon thin-film solar cells. *Ceram Int*. 2017;43(12):9382-9.
21. Fang GJ, Li D, Yao BL. Influence of post-deposition annealing on the properties of transparent conductive nanocrystalline ZAO thin films prepared by RF magnetron sputtering with highly conductive ceramic target. *Thin Solid Films*. 2002;418(2):156-62.
22. Zhu K, Wang H, Xiao F, Xu F. Effect of buffer thickness on the properties of Al-doped ZnO thin films prepared by DC magnetron sputtering. *J Mater Sci Mater Electron*. 2017;28(10):7302-6.
23. Chen M, Pei ZL, Sun C, Wen LS, Wang X. Surface characterization of transparent conductive oxide Al-doped ZnO films. *J Cryst Growth*. 2000;220:254-62.
24. Bortoleto JRR, Chaves M, Rosa AM, Da Silva EP, Durrant SF, Trino LD, et al. Growth evolution of self-textured ZnO films deposited by magnetron sputtering at low temperatures. *Appl Surf Sci*. 2015;334:210-5.
25. Tondare RS, Shivaraj BW, Narasimhamurthy HN, Krishna M, Subramanyam TK. Effect of deposition time on structural, electrical and optical properties of Aluminium doped ZnO thin films by RF magnetron sputtering. *Mater Today*. 2018;5:2710-5.
26. Cullity BD, Stock SR. Elements of x-ray diffraction. 3rd ed. London: Pearson; 2001. 678 p.
27. Tauc J. Optical properties and electronic structure of amorphous Ge and Si. *Mater Res Bull*. 1968;3(1):37-46.
28. Fox M. Optical properties of solids. 2nd ed. Cary: Oxford Press; 2010. 415 p.
29. da Silva ÉP, Chaves M, Durrant SF, Lisboa-Filho PN, Bortoleto JRR. Morphological and electrical evolution of ZnO:Al thin films deposited by RF magnetron sputtering onto glass substrates. *Mater Res*. 2014;17:1384-90.
30. Grundmann M. The physics of semiconductors - an introduction including nanophysics and applications. 2nd ed. USA: Springer Science; 2010. 690 p.
31. Wang F, Wu MZ, Wang YY, Yu YM, Wu XM, Zhuge LJ. Influence of thickness and annealing temperature on the electrical, optical and structural properties of AZO thin films. *Vacuum*. 2013;89:127-31.
32. Dong BZ, Fang GJ, Wang JF, Guan WJ, Zhao XZ. Effect of thickness on structural, electrical, and optical properties of ZnO:Al films deposited by pulsed laser deposition. *J Appl Phys*. 2007;101:033713.
33. Kajikawa Y. Texture development of non-epitaxial polycrystalline ZnO films. *J Cryst Growth*. 2006;289(1):387-94.
34. Novák P. Possibilities of Increasing the usability of sputtered AZO films as a transparent electrode. *Phys Status Solidi (A)*. 2019;216(7):1800814.
35. Yu X, Ma J, Ji F, Wang Y, Cheng C, Ma H. Thickness dependence of properties of ZnO:Ga films deposited by rf magnetron sputtering. *Appl Surf Sci*. 2005;245:310-5.
36. Patel TA, Singh CC, Panda E. Microstructure influenced variation in the local surface electrical heterogeneity in thickening Al-doped ZnO films: evidence using both scanning tunnelling spectroscopy and conductive atomic force microscope. *Mater Sci Semicond Process*. 2018;75:65-74.
37. Cornelius S, Vinnichenko M. Al in ZnO - From doping to alloying: an investigation of Al electrical activation in relation to structure and charge transport limits. *Thin Solid Films*. 2016;605:20-9.
38. Bikowski A, Ellmer K. Analytical model of electron transport in polycrystalline, degenerately doped ZnO films. *J Appl Phys*. 2014;116:143704.
39. Horwat D, Jullien M, Capon F, Pierson JF, Andersson J, Endrino JL. On the deactivation of the dopant and electronic structure in reactively sputtered transparent Al-doped ZnO thin films. *J Phys D Appl Phys*. 2010;43:18-22.
40. Yoshioka S, Oba F, Huang R, Tanaka I, Mizoguchi T, Yamamoto T. Atomic structures of supersaturated ZnO-Al₂O₃ solid solutions. *J Appl Phys*. 2008;103(1):014309.